PAPER

Superconducting HfO₂-added solution-derived YBa₂Cu₃O₇ nanocomposite films: the effect of colloidal nanocrystal shape and crystallinity on pinning mechanism

To cite this article: H Rijckaert et al 2022 Supercond. Sci. Technol. 35 084008

View the article online for updates and enhancements.

You may also like

- Rules of non-superconducting phase particles on crack propagation in YBCO coated conductors fabricated by the IBAD-
- Lei Shen, Cong Liu and Xingyi Zhang
- The influence of BaSnO₂ and BaZrO₂ nanoinclusions on the critical current and local structure of HTS coated conductors A P Menushenkov, A A Ivanov, O V Chernysheva et al.
- Size-controlled spontaneously segregated Ba, YTaO, nanoparticles in YBa, Cu, O, nañocomposites obtained by chemical solution deposition

 M Coll, R Guzman, P Garcés et al.



IOP ebooks™

Bringing together innovative digital publishing with leading authors from the global scientific community.

Start exploring the collection-download the first chapter of every title for free.

Supercond. Sci. Technol. 35 (2022) 084008 (8pp)

https://doi.org/10.1088/1361-6668/ac7ae3

Superconducting HfO₂-added solution-derived YBa₂Cu₃O₇ nanocomposite films: the effect of colloidal nanocrystal shape and crystallinity on pinning mechanism

H Rijckaert^{1,*}, M Malmivirta², S Banerjee³, S J L Billinge^{3,4}, H Huhtinen², P Paturi², K De Buysser¹ and I Van Driessche¹

E-mail: Hannes.Rijckaert@UGent.be

Received 1 June 2022 Accepted for publication 21 June 2022 Published 30 June 2022



Abstract

Two different types of monoclinic HfO_2 nanocrystals were employed in this work to study the effect of nanocrystal shape and crystallinity on the structural defects in the YBa2Cu3O7- δ (YBCO) matrix as it leads to an enhancement of pinning performances of solution-derived YBCO nanocomposite films. In this work the nanorod-like HfO_2 nanocrystals obtained from surfactant-controlled synthesis led to short intergrowths surrounding the particles, while spherical HfO_2 nanocrystals from the solvent-controlled synthesis led to the formation of long stacking faults in the YBCO matrix. It means that the small difference in crystallinity, lattice parameters, nanocrystal structures, core diameter of preformed nanocrystals in colloidal solutions have a strong influence on the formation of the structural defects around the particles in the YBCO matrix, leading to different pinning performances.

Supplementary material for this article is available online

Keywords: CSD, nanocomposite, nanoparticles, pinning, thin film, superconductor, YBCO

1

(Some figures may appear in colour only in the online journal)

¹ SCRiPTS, Department of Chemistry, Ghent University, Krijgslaan 281-S3, 9000 Ghent, Belgium

² Wihuri Physical Laboratory, Department of Physics and Astronomy, University of Turku, 20014 Turku, Finland

³ Department of Applied Physics and Applied Mathematics, Columbia University, 1105 S.W. Mudd, New York, NY 10027, United States of America

⁴ Condensed Matter Physics and Materials Science Department, Brookhaven National Laboratory, Upton, NY 11973, United States of America

^{*} Author to whom any correspondence should be addressed.

1. Introduction

The chemical solution deposition (CSD) pathway to fabricate and to optimize $REBa_2Cu_3O_{7-\delta}$ (RE = rare earth, REBa2Cu3O7 $-\delta$ (REBCO)) nanocomposite films with relevant pinning properties does not seem straightforward due to the necessity to solve several critical issues related to nanoparticle formation as artificial pinning centers in the REBCO matrix [1]. This non-vacuum and cost-effective solution-derived method is considered to be one of the attractive routes for the fabrication of coated conductors [2, 3]. This method has the advantages to achieve a large film thickness, to create a multilayer architecture and to generate a nanocomposite film via colloidal or (multi-)metal precursor solutions [3–6]. However, starting with multi-metal precursor solutions shows the limited control and reproducibility of the formation and the size distribution of self-assembled nanoparticles (in-situ approach) in the REBCO matrix. An alternative pathway, starting with colloidal solutions that consist of preformed nanocrystals (exsitu approach), has shown the possibility to improve reproducibility as well as the control over the particle composition and size in the REBCO matrix. Some attempts were already made with several preformed nanocrystals, yielding solutionderived REBCO nanocomposite films with successful increase of the pinning force densities [7, 8]. But these pinning force densities are still low compared to pulsed laser deposition and metal-organic chemical vapor deposition based REBCO nanocomposites. The enhancement of pinning force density in the low-fluorine (YBCO) nanocomposite films starting from preformed nanocrystals thus becomes an important goal.

In our previous work [8, 9], it has been shown that the nanocrystal surface chemistry and appropriate ligand play a fundamental role during the nanocomposite formation and determine the final superconducting properties. Despite all the approaches mentioned above, there is some lack of understanding the influence of colloidal nanocrystal shape and crystallinity on the microstructure formation of the CSD-based YBCO nanocomposite film. In this work, two different non-aqueous approaches to synthesize HfO2 nanocrystals (surfactant- and solvent-controlled process) were employed to study the influence of nanocrystal shape and crystallinity on the defect landscape of the YBCO matrix. In the surfactantcontrolled process, the metal precursors are transformed to oxide compounds in the presence of stabilizing ligands. Here, the solvothermal heating-up (HU, surfactant-controlled) synthesis yielded highly crystalline nanorod-like HfO₂ nanocrystals with a diameter of 2.6 nm and length of 8.0 nm. This surfactant-controlled approach can offer better control over the crystal size and shape with a low agglomeration tendency as the present surfactant is able to cap the nanocrystals' surfaces [10]. Alternatively, the solvent-controlled process uses a surfactant-free environment. This approach is simpler compared to the surfactant-controlled process, as only two components (metal precursor and solvent) are present in the reaction mixture, simplifying the elucidation of the reaction mechanism. In general, the solvent-controlled approach results in particle agglomeration, although the dispersibility can be improved via a post-synthetic surface functionalization step. Here we employ a microwave (MW)-assisted (solvent-controlled) synthesis which delivers highly crystalline HfO_2 nanocrystals with a spherical shape and a diameter of 6–8 nm.

With these two types of monoclinic HfO₂ nanocrystals, the effect of the nanocrystal shape and crystallinity on the YBCO matrix can be studied. This work shows that the nanorod-like HfO₂ nanocrystals obtained from surfactant-controlled synthesis led to short intergrowths surrounding the particles while spherical HfO₂ nanocrystals from the solvent-controlled synthesis led to the formation of long stacking faults in the YBCO matrix. Therefore, the differences in the nanocrystal shape and crystallinity due to the different nanocrystal synthesis approach has a strong influence on the formation of the intergrowths and the line defects around the particles in the YBCO matrix, leading to different pinning performances.

2. Methods

2.1. Nanocrystal preparation

The HU synthesis of HU-HfO₂ nanocrystals was adapted from De Keukeleere *et al* [11]. These as-synthesized HfO₂ nanocrystals are redispersed in toluene, yielding a clear suspension. To achieve a stable colloidal YBCO solution, the nanocrystals are transferred to methanol via the addition of a polar copolymer with phosphonate groups. MW-HfO₂ nanocrystals are synthesized via a MW-assisted solvothermal treatment as described by De Roo *et al* [12]. After the MW-assisted synthesis, MW-HfO₂ nanocrystals are post-functionalized with dodecanoic acid and oleyl amine, yielding a clear suspension in chloroform. The ligand exchange with glutamine and copolymer with phosphonate group is introduced to transfer these nanocrystals to colloidal YBCO solution. More experimental details are described in supplementary material.

2.2. Nanocrystal characterization

The nanocrystal shape was studied by transmission electron microscopy (TEM, JEOL JEM-2000FS operated at 200 kV) and the nanocrystal core dimension was measured from the TEM images (more than 100 nanocrystals) via the image processing software ImageJ. The solvodynamic diameter of HfO₂ nanocrystals was determined via dynamic light scattering (DLS) analysis on a Malvern Nano ZS in backscattering mode (173°). The x-ray diffraction (XRD) data were collected on a Thermo Scientific ARL X'tra diffractometer equipped with a Peltier cooled detector. Samples were measured in θ –2 θ geometry over the angular range 20° – 80° (2θ) (Cu K α radiation) using a 0.02° 2θ step size and 1 s/step counting time. The Rietveld method for whole-powder pattern fitting was used, and TOPAS-Academic V4.1 software [13] was used for Rietveld refinement. Total scattering pair distribution function (PDF) experiments were performed at the National Synchrotron Light Source II (XPD, 28-ID2), Brookhaven National Laboratory. The dried HfO₂ nanopowders were loaded in polyimide capillaries and diffraction patterns were collected at room temperature in a transmission geometry with an x-ray energy of 66.47 keV ($\lambda=0.1854$ Å) using a large area 2D PerkinElmer detector with a sample-to-detector distance of 202.99 mm. The experimental setup was calibrated by measuring a crystalline Ni powder. The program PDFgetX3 [14] within xPDFsuite [15] was used to perform standardized corrections to obtain the reduced total scattering structure function F(Q), and Fourier transformation to obtain the PDF. The data are shown in figure S3 (supplementary information). The PDFgui [16] program was used to construct virtual crystal nanoparticle models from reference structures, carry out refinements, and determine the agreement between calculated PDFs and data, quantified by the residual.

2.3. CSD and thermal treatment

YBCO precursor solution is prepared by dissolving barium trifluoroacetate, copper propionate and yttrium propionate with a Y:Ba:Cu ratio of 1:2:3 and a total concentration of 1.08 M l⁻¹ in methanol. The HfO₂ nanocrystals are added with a concentration of 5 mol-% into YBCO precursor solutions. We have chosen this concentration based on our previous results on ZrO₂-added YBCO nanocomposite films [8]. The (100)-oriented LaAlO₃ single-crystalline substrates were spincoated with 2000 rpm for 1 min and then dried at 65 °C on a hotplate for 5 min in ambient atmosphere. The dried coated substrates were pyrolyzed by heating to 400 °C with heating rate of 3 °C-5 °C min⁻¹ in a wet O₂ atmosphere. The pyrolyzed YBCO films were heated up to 795 °C with an intermediate dwelling step at 640 °C to crystallize YBCO under wet N₂ atmosphere and an O₂ partial pressure of 100 ppm. More experimental details are described in [17].

2.4. Structural characterization

The XRD measurements were investigated by Philips Xpert Pro (Cu- K_{α}) diffractometer with Schulz texture goniometer to characterize the phase composition and texture of the YBCO films. Cross-sectional TEM lamella was prepared using ion milling techniques via the focused ion beam *in-situ* lift-out procedure. Scanning TEM (STEM) analysis of HfO₂-added YBCO films was investigated with FEI Titan QuantEM probe corrected microscope, allowing an extremely high resolution in STEM-mode operated at 300 kV. The software ImageJ was used to obtain the mean size diameter of the particles in cross-sectional areas.

2.5. Electrical characterization

The superconducting properties of the YBCO films were characterized via the transport critical current measurements in a Quantum Design Physical Property Measurement System. The YBCO films were photolithographically etched to $90 \pm 5~\mu m$ wide stripes with a solution of 0.15 M phosphoric acid in deionized water. The thicknesses and exact widths of the stripes, needed for the critical current density J_c values, were determined by atomic force microscopy after etching. The etched pattern was a standard four-probe measurement circuit

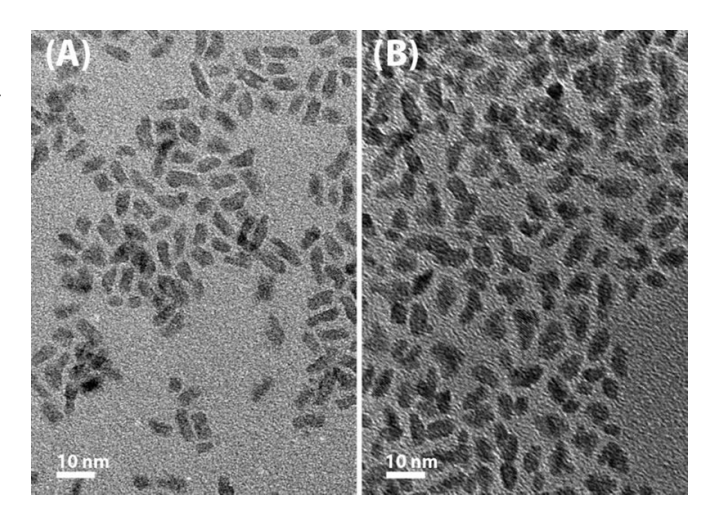


Figure 1. TEM image of (A) HU-based and (B) MW-based HfO₂ nanocrystals.

where the contacts on these samples were made by tapping with indium. The values for voltage between the voltage pads as a function of the applied current were recorded with the electric field criterion of $215 \mu V \text{ cm}^{-1}$.

3. Results and discussion

As illustrated in figure 1, HU-HfO2 synthesis delivers an average nanocrystal core of 2.6 nm in diameter and 8.0 nm in length which looks like a very small nanorod, while MW-HfO₂ synthesis yields more spherical nanocrystals with an average nanocrystal diameter of 6-8 nm. The solvodynamic diameter of both HfO₂ nanocrystals are in same range of 10-11 nm (see table 1). The difference between nanocrystal core dimension and solvodynamic diameter corresponds to the stabilization ligand and solvation shell. The PDF measurements gives the average size of the crystallite core size (structural coherence length) of 3.6 nm for HU-HfO₂ and 4.3 nm for MW-HfO₂. It means that both (surfactant- and solvent-controlled) types of synthesis delivered different nanocrystal shapes and degree of nanocrystalline order (crystallinity). The PDF analysis also gives further quantitative insight into the nanocrystal structure. Best fits to the data confirmed that the monoclinic HfO2 structure in the $P2_1/c$ space-group [18] is clearly preferred over either orthorhombic or cubic HfO₂ structural variants. The fits, shown in figure S4 (supplementary information), revealed that the MW-HfO2 nanocrystals had a higher degree of structural order and fewer defects. Despite being in physically smaller nanocrystals based on TEM evidence, the range of structural coherence of the crystallites was 20% higher in the MW-HfO₂ than the HU-HfO₂ nanocrystals and the PDF peaks were slightly sharper, reflected in a small refined value for the Hf atomic displacement parameters $(0.004 \text{ A}^2 \text{ vs. } 0.007 \text{ A}^2,$ respectively). Rietveld refinements on both types of HfO2 nanocrystals show a slightly difference in the lattice parameters where the unit cell of HU-HfO₂ nanocrystals is slightly longer compared to the MW-HfO₂. This result was further supported by the PDF refinements. YBCO has an orthorhombic

Table 1. Overview of nanocrystal core dimension via TEM, solvodynamic diameter size in methanol via DLS, crystallite core size (structural coherence length) via PDF, and lattice parameter via Rietveld refinements of HU-based and MW-based HfO₂ nanocrystals.

HfO ₂ nanocrystals	Nanocrystal core dimension	Solvodynamic diameter	Crystallite core size	Lattice parameter
HU-based	2.6 nm in diameter 8.0 nm in length	10.7 nm	3.6 nm	a = 5.175(21) Å b = 5.170(21) Å c = 5.328(17) Å
MW-based	6–8 nm in diameter	11.0 nm	4.3 nm	a = 5.192(16) Å b = 5.182(14) Å c = 5.318(14) Å

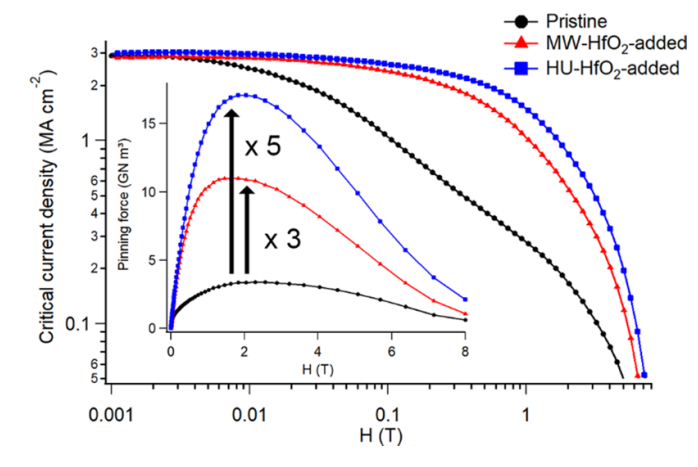


Figure 2. $J_c(H)$ dependency for pristine, HU- HfO_2 -added and MW- HfO_2 -added YBCO films and their corresponding pinning force densities (inset) at 77 K.

structure with lattice parameters a = 3.82 Å, b = 3.88 Å and c/3 = 3.89 Å [19]. Therefore, $a \sim b \sim c/3 \approx 3.86$ Å, which suggests that MW-HfO₂ nanocrystals would be better matched to the YBCO structure compared to HU-HfO₂ nanocrystals.

These pristine, HU-HfO₂-added and MW-HfO₂-added YBCO precursor solutions were spin-coated on LaAlO₃ substrate. After a crystallization step, the J_c of all films are within the scope of 2.8-3 MA cm⁻² at 77 K. The transport measurements (figure 2) show that both HfO2-added YBCO films present a smoother J_c dependency with the magnetic field compared to pristine YBCO. This indicates that the addition of preformed HfO₂ nanocrystals improves the pinning performances. The HU-HfO₂-added YBCO film (blue line) shows a later J_c decay compared to the MW-HfO₂-added YBCO film (red line). On the other hand, it also shows an increase of a factor of five of maximum of pinning force density (F_p^{max}) of 17.11 GN m^{-3} at 2.1 T, inset figure 2) compared to pristine YBCO films (F_p^{max} of 3.40 GN m⁻³ at 2.2 T) at 77 K. Nevertheless, MW-HfO2-added YBCO films show a threefold increase of F_p^{max} to 11.04 GN m⁻³ at 1.6 T with respect to the pristine film.

In order to explain why the HU-based HfO₂ nanocrystals show better pinning force densities compared to MW-based HfO₂ nanocrystals, the microstructure of the films was studied by taking STEM images of the cross sections of the obtained thin films. Figures 3(a) and (b) show the overview

of HU-HfO2-added and MW-HfO2-added YBCO nanocomposite films. In both STEM images, a homogenous distribution of BaHfO3 particles was observed into the YBCO matrix with a difference in area density of stacking faults (black lines in figures 3(a) and (b)). It is clear that MW-HfO2added film has higher area density of stacking faults compared to HU-HfO₂-added film. The formation and coarsening of BaHfO₃ particles in the YBCO matrix is due to the reactivity of HfO2 nanocrystals with Ba2+ during the crystallization. The STEM image of a HU-HfO2-added YBCO film, figure 3(a), shows BaHfO₃ particles embedded in the YBCO matrix with mean size diameter of 12.2 \pm 2.8 nm. Smaller-sized nanoparticles result in a higher number density of nanoparticles (table 2) in the YBCO matrix. However, some agglomerations of BaHfO₃ particles, which lead to larger particles, can be also occasionally observed (figures 3(a) and (c)). On the other hand, the BaHfO₃ particles in the MW-HfO₂-added YBCO film exhibit slightly larger mean diameter (17.8 \pm 5.6 nm) (cf figure 3(b)). These high-angle annular dark-field (HAADF) STEM images of the BaHfO₃ particles reveal no particular crystallographic relation between the BaHfO₃ and the YBCO matrix. As described in the work of Molina-Luna et al [20], misfit interfacial dislocations with a distance less than 2 nm are usually observed at the BaHfO₃/YBCO interface in CSD-grown films, which can act as nucleation centers for Ba-Cu-Cu-Ba (Y124-type) stacking faults. A closer look into the HU-HfO2-added YBCO microstructure (figures 3(c) and (d)) reveals a 1 nm dark amorphous region at the interface between BaHfO₃ particles and the YBCO matrix (figure 3(d)). This is due to the incoherent interface and the induced YBa₂Cu₄O₈ (Y124) structural defects, which consist of an intergrowth of an extra Cu-O chain layer. It has been observed that randomly oriented BaHfO₃ particles are surrounded by large clusters of Y124 intergrowths, which means that all YBCO unit cells exhibit an additional Cu-O layer. This intergrowth is also observed in self-assembled YBCO-BaZrO₃ nanocomposite film with small 10-20 nm nanoparticles, promoting short intergrowths. These short intergrowths can act as effective pinning centers [21, 22] explaining why this film is the one with the best superconducting properties measured in this work. On the other hand, the larger BaHfO₃ particles (17.8 \pm 5.6 nm, figure 3(e)) present in the MW-HfO₂-added YBCO film lead to a reduction of the incoherent interface and this results in the formation of longer stacking faults. This means that an extra Cu-O

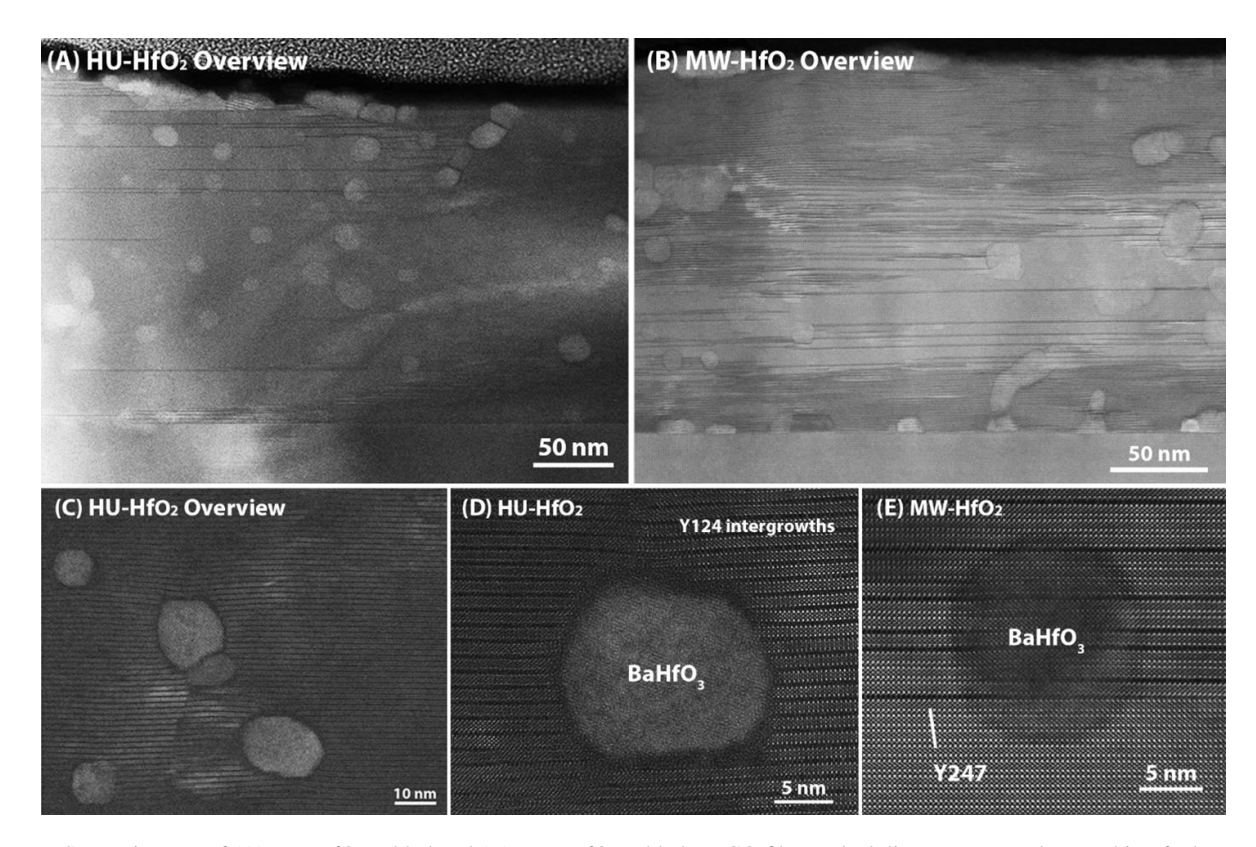


Figure 3. STEM images of (A) HU-HfO₂-added and (B) MW-HfO₂-added YBCO films. Black lines correspond to stacking faults. (C) STEM overview image of HU-HfO₂-added YBCO microstructure, showing a 1 nm dark region around the particles and (D) isolated BaHfO₃ particles surrounded with Y124 intergrowths. (E) HAADF-STEM image of MW-HfO₂-added YBCO microstructure shows the stacking faults are produced around the particles.

Table 2. Critical current densities J_c and maximum pinning force densities F_p^{max} at 77 K of pristine, HU-HfO₂-added and MW-HfO₂-added YBCO films. The summary of the mean size diameter, number density and volume fraction of particles in the YBCO matrix for the both HfO₂-added YBCO films.

HfO ₂ nanocrystals	$J_{\rm c}$ (0) at 77 K (MA cm ⁻²)	$F_{\rm p}^{\rm max}$ (77 K) (GN m ⁻³)	Mean size diameter in the YBCO matrix (nm)	Number density of particle ($\times 10^3$ in μ m ⁻³ YBCO)	Volume fraction of particles in the YBCO matrix
Pristine	2.92	3.40	_	_	_
HU-based	3.04	17.11	12.2 ± 2.8	26	4.7%
MW-based	2.88	11.04	17.8 ± 5.6	8	4.5%

layer is introduced in every two YBCO unit cells. So, the large stacking faults seem to be produced by the reduction of the incoherent interface, which would degrade the critical current densities [23, 24]. It is important to control Y124 intergrowths and Y247 stacking faults as they can result in negative effects on J_c [23, 25, 26]. It is worth noting that HU-based HfO2 nanocrystals show an improvement of $F_p^{\rm max}$ of a factor of five compared to HU-based ZrO2 nanocrystals in YBCO nanocomposite (a factor of three) [17]. In previous works [8, 9, 17], spherical HU-based ZrO2 nanocrystals with distorted tetragonal crystal structure with a crystallize domain size of 3.9 nm (as confirmed via PDF measurements) was introduced in the YBCO matrix. The incorporation of these HU-based ZrO2 nanocrystals yielded in 13.0 ± 5.5 nm BaZrO3 particles in the YBCO matrix. These BaZrO3 particles are randomly oriented

with a small incoherent interface, leading to no formation of stacking faults around BaZrO₃ particles [8]. It contains volume number density of 25×10^3 BaZrO₃ particles in μ m⁻³ YBCO volume and thus a volume fraction of $\sim 5.5\%$. As the volume fraction is in the same range as HfO₂-added films (table 2), it gives an indication that the combination of the volume fraction of non-superconducting particles and the stacking fault area density is important key to control the flux pinning properties.

In XRD studies of the films, it was observed that the addition of HfO_2 nanocrystals in the YBCO matrix does not essentially change the c-lattice parameters and all (00l) peaks show single peak (figure S5 in supporting information). On the other hand, in the rocking curve of the (005) peak (figure 4), all films clearly show two overlapping peaks, one very narrow and one wide. The proportion of the integrated intensity of

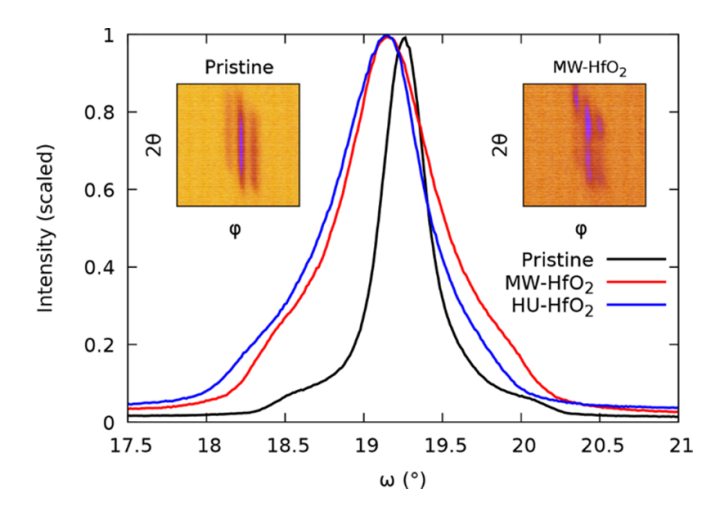


Figure 4. The rocking curves of the (005) peaks of all the films. The increase of the intensity of the wide part is clearly seen. The insets show the 2θ - ϕ scans of the (122)/(212) peak sets for the pristine and the MW-HfO₂-added films. The HU-HfO₂-added film has similar split in the direction of the peaks. The split in ϕ indicates normal twin structure in the films.

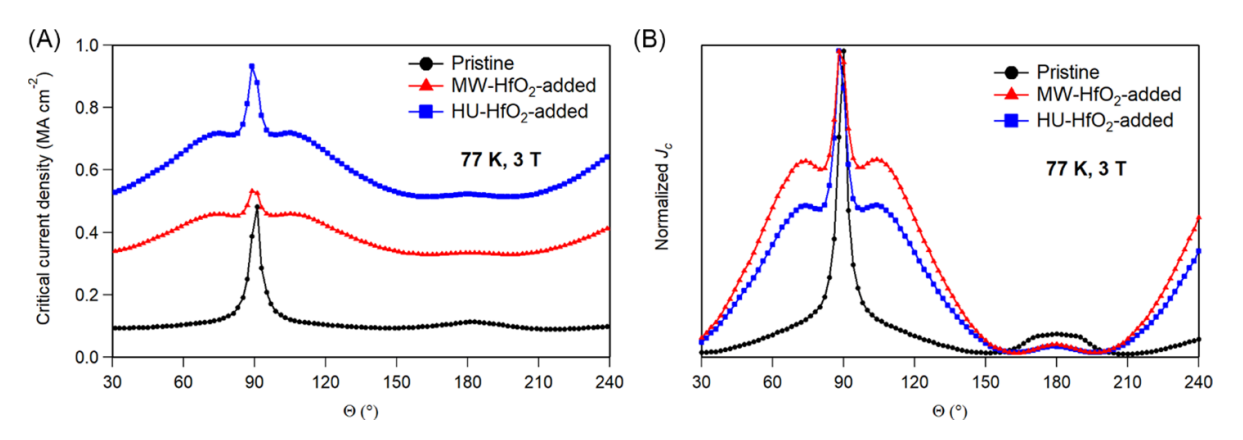


Figure 5. Angular dependence of J_c in (a) absolute and normalized (b) to [0, 1] value measured at 77 K and 3 T of pristine and HfO₂-added films.

the wide peak increases from about 50% to 70% by the addition of nanocrystals. Since the widening of the rocking curve is due to the mosaic spread of the unit cells, we can connect this widening to the bending of the Cu–O layers around the BaHfO₃ particles in the YBCO matrix seen e.g. in figure 3(d). Also, it is observed that the twin structure is normal in all films (figure 4 insets), but the HfO₂-added films splits the peaks in the 2θ direction. In the pristine film, the (122)/(212) peaks are very strained and the peak width is around 0.8°, whereas in the HfO₂-added films the peak width is 0.45°. This division and release of strain can be due to the increased amount of Y124 and Y247 intergrowths.

Figure 5(a) shows the dependence of J_c with the magnetic field orientation at 77 K and 3 T for pristine and HfO₂-added films in absolute value while figure 5(b) shows the normalized to [0, 1] values. It is clear that both HfO₂-added films show an increase of the absolute J_c in the whole angular range as well as a more isotropic behavior than the pristine YBCO film due to the overall enhanced pinning caused by the spherical and randomly distributed BaHfO₃ particles. Both HfO₂-added YBCO films also show the overall broadness of the ab-peak ($\Theta = 90^{\circ}$)

which can be explained by the presence of stacking faults and other in-plane defects induced by the BaHfO₃ particles. The stacking faults are perfectly aligned with the ab-plane and therefore the shoulders on both sides of the ab-peak are more related to the size and distributions of the BaHfO₃ particles it. The MW-HfO₂-added film shows lower J_c values around abpeak compared to the HU-HfO₂-added film due to the difference in number density of particles and area density of stacking faults. Its values are however larger than in the case of the pristine YBCO film. On the other hand the increase of stacking fault area density, caused by the addition of nanocrystals, results in a decrease of the vertical coherence of the twin boundaries along the c-axis ($\Theta = 180^{\circ}$), which explains the less pronounced c-peak visible in HfO₂-added films when compared to the pristine YBCO film in normalized value (figure 5(b), also confirmed in figure 4 where pristine YBCO film show better vertical coherence in *c*-direction).

As observed in previous work [17], the F_p^{max} values of ZrO₂-added YBCO films were only increased with factor of three compared to pristine YBCO films, which may be explained by the absence of stacking faults around the BaZrO₃

particles and in the YBCO matrix. We are strongly convinced that the pinning properties could be further improved by combining the addition of preformed nanocrystals and the formation of short stacking faults around the particles. Shorter stacking faults are more effective as pinning centers because they cause more dislocations (the real pinning center) per unit of area. The formation of stacking faults can be originated from the decomposition of Cu-containing impurity phases (such as Ba–Cu–O) during the oxygenation process [27–29], a follow-up research should be carried out varying the oxygenation temperature to increase the stacking faults density in the YBCO matrix with nanocrystals. We are also convinced that the type of nanocrystals (composition, shape, crystallinity, ...) play a role during the formation of stacking faults. Also, the introduction of the double metal oxide nanocrystals, such as BaHfO₃ and BaZrO₃ can avoid the coarsening or agglomerations of particles during the YBCO growth, resulting in smaller particles, which acts as nucleation centers for formation of stacking faults [30]. Thus, the key parameter to control this combination of formation of short stacking faults/intergrowths (area density of stacking faults) and agglomeratefree nanocrystals (volume fraction of particles) with a size range in diameter of 5-10 nm in the YBCO matrix is the type of nanocrystals and its crystallinity. This should lead to an enhancement of pinning performances of YBCO nanocomposite films.

4. Conclusion

In this work, two different methods (surfactant- and solventcontrolled) to synthesize HfO2 nanocrystals were employed to investigate the influence of nanocrystal shape and crystallinity on the defect state of the YBCO matrix. The solvothermal HU (or surfactant-controlled) synthesis yielded nanorod-like HfO₂ nanocrystals with a core dimension of 2.6 nm in diameter and 8.0 nm in length. The MW-assisted (or solventcontrolled) synthesis delivered spherical HfO2 nanocrystals with a core dimension of 6-8 nm in diameter. These two types of monoclinic HfO₂ nanocrystals also show small difference in crystallinity, lattice parameters, and crystallite core, which lead to the different formation of the structural defects around the particles in the YBCO matrix. With this solution-derived approach, it has been shown that the colloidal nanocrystal shape and crystallinity are the key parameters for better control of the structural defects in the YBCO matrix. Particles with incoherent interface in the YBCO matrix would promote the formation of small planar defects (stacking faults) around the particles in the YBCO matrix, increasing the pinning force densities. On the other hand, particles with coherent interface in the YBCO matrix lead to formation of larger stacking faults resulting to decrease of the superconducting properties. These results show that preformed nanocrystals with different shape and crystalline offer the opportunities to control the particle distribution (volume fraction) and to tune the formation of structural defects (area density) in the YBCO matrix. Therefore, we expect that the relationship between the type of colloidal nanocrystal and the final nanocomposite performance will also be relevant for the further development of solution-derived *REBCO* nanocomposite research.

Data availability statement

The data that support the findings of this study are available upon reasonable request from the authors.

Acknowledgments

This work was financially supported by the European Union Horizon 2020 Marie Curie Actions under the project SynFoNY (H2020/2016-722071). H R acknowledges support and funding as postdoctoral fellow fundamental research of the Research Foundation—Flanders (FWO) under Grant No. 1273621N. P P and H H wish to thank the Jenny and Antti Wihuri Foundation for financial support. PDF analysis in the S J L B group was supported by the US National Science Foundation through Grant DMREF-1922234. X-ray PDF measurements were conducted on beamline 28-ID-1/28-ID-2 of the National Synchrotron Light Source II, a US Department of Energy (DOE) Office of Science User Facility operated for the DOE Office of Science by Brookhaven National Laboratory under Contract No. DE-SC0012704. The authors thanks Dr N Gauquelin (University of Antwerp) for TEM measurements.

ORCID iDs

H Rijckaert https://orcid.org/0000-0002-6078-2919
H Huhtinen https://orcid.org/0000-0002-2166-5939
P Paturi https://orcid.org/0000-0002-6240-2801
I Van Driessche https://orcid.org/0000-0001-5253-3325

References

- [1] Puig T, Gutiérrez J, Pomar A, Llordés A, Gazquez J, Ricart S, Sandiumenge F and Obradors X 2008 Vortex pinning in chemical solution nanostructured YBCO films Supercond. Sci. Technol. 21 034008
- [2] Obradors X and Puig T 2014 Coated conductors for power applications: materials challenges Supercond. Sci. Technol. 27 044003
- [3] Díez-Sierra J, Rijckaert H, Rikel M, Hänisch J, Sadewasser M, Koliotassis L, Meledin A, López-Domínguez P, Falter M and Bennewitz J 2021 All-chemical YBa₂Cu₃O_{7-δ} coated conductors with preformed BaHfO₃ and BaZrO₃ nanocrystals on Ni5W technical substrate at the industrial scale Supercond. Sci. Technol. 34 114001
- [4] Pop C, Villarejo B, Pino F, Mundet B, Ricart S, de Palau M, Puig T and Obradors X 2018 Growth of all-chemical high critical current YBa₂Cu₃O_{7-δ} thick films and coated conductors Supercond. Sci. Technol. 32 015004
- [5] Rijckaert H, Cayado P, Nast R, Diez Sierra J, Erbe M, López Dominguez P, Hänisch J, De Buysser K, Holzapfel B and Van Driessche I 2020 Superconducting HfO₂-YBa₂Cu₃O_{7-δ} nanocomposite films deposited using ink-jet printing of colloidal solutions *Coatings* 10 17
- [6] Villarejo B, Pino F, Pop C, Ricart S, Valles F, Mundet B, Palau A, Roura-Grabulosa P, Farjas J and Chamorro N 2021 High performance of superconducting YBa₂Cu₃O₇ thick

- films prepared by single-deposition inkjet printing ACS Appl. Electron. Mater. 3 3948–61
- [7] Cayado P et al 2015 Epitaxial YBa₂Cu₃O_{7-x} nanocomposite thin films from colloidal solutions Supercond. Sci. Technol. 28 124007
- [8] Rijckaert H et al 2017 Optimizing nanocomposites through nanocrystal surface chemistry: superconducting YBa₂Cu₃O₇ thin films via low-fluorine metal organic deposition and preformed metal oxide nanocrystals Chem. Mater. 29 6104–13
- [9] Rijckaert H, De Roo J, Van Zele M, Banerjee S, Huhtinen H, Paturi P, Bennewitz J, Billinge S, Bäcker M and De Buysser K 2018 Pair distribution function analysis of ZrO₂ nanocrystals and insights in the formation of ZrO₂-YBa₂Cu₃O₇ nanocomposites *Materials* 11 1066
- [10] Niederberger M and Pinna N 2009 Metal Oxide Nanoparticles in Organic Solvents: Synthesis, Formation, Assembly and Application (London: Springer)
- [11] De Keukeleere K, Coucke S, De Canck E, Van Der Voort P, Delpech F, Coppel Y, Hens Z, Van Driessche I, Owen J S and De Roo J 2017 Stabilization of colloidal Ti, Zr, and Hf oxide nanocrystals by protonated Tri-n-octylphosphine oxide (TOPO) and its decomposition products *Chem. Mater.* 29 10233–42
- [12] De Roo J, De Keukeleere K, Feys J, Lommens P, Hens Z and Van Driessche I 2013 Fast, microwave-assisted synthesis of monodisperse HfO₂ nanoparticles J. Nanopart. Res. 15 1778
- [13] Coelho A A 2018 TOPAS and TOPAS-Academic: an optimization program integrating computer algebra and crystallographic objects written in C++ *J. Appl. Crystallogr.* 51 210–8
- [14] Juhás P, Davis T, Farrow C L and Billinge S J 2013 PDFgetX3: a rapid and highly automatable program for processing powder diffraction data into total scattering pair distribution functions J. Appl. Crystallogr. 46 560-6
- [15] Yang X, Juhas P, Farrow C L and Billinge S J 2014 xPDFsuite: an end-to-end software solution for high throughput pair distribution function transformation, visualization and analysis (arXiv:1402.3163)
- [16] Farrow C, Juhas P, Liu J, Bryndin D, Božin E, Bloch J, Proffen T and Billinge S 2007 PDFfit2 and PDFgui: computer programs for studying nanostructure in crystals J. Phys: Condens. Matter 19 335219
- [17] Rijckaert H, Hänisch J, Pollefeyt G, Bäcker M and Van Driessche I 2019 Influence of Ba²⁺ consumption and intermediate dwelling during processing of YBa₂Cu₃O₇ nanocomposite films J. Am. Ceram. Soc. 102 3870–8
- [18] Ruh R and Corfield P W 1970 Crystal structure of monoclinic hafnia and comparison with monoclinic zirconia *J. Am. Ceram. Soc.* 53 126–9

- [19] Konishi M, Wen J, Fuke H, Matsunaga Y, Hayashi K, Odagawa A, Enomoto Y, Sakai H, Yamada Y and Koyama S 1995 Homoepitaxial growth of YBCO thin films an YBCO single crystals *IEEE Trans. Appl. Supercond.* 5 1229–32
- [20] Molina-Luna L, Duerrschnabel M, Turner S, Erbe M, Martinez G T, Van Aert S, Holzapfel B and Van Tendeloo G 2015 Atomic and electronic structures of BaHfO₃-doped TFA-MOD-derived YBa₂Cu₃O_{7-δ} thin films Supercond. Sci. Technol. 28 115009
- [21] Gutierrez J, Llordes A, Gazquez J, Gibert M, Roma N, Ricart S, Pomar A, Sandiumenge F, Mestres N and Puig T 2007 Strong isotropic flux pinning in solution-derived YBa₂Cu₃O_{7-x} nanocomposite superconductor films *Nat. Mater.* 6 367-73
- [22] Guzman R, Gazquez J, Mundet B, Coll M, Obradors X and Puig T 2017 Probing localized strain in solution-derived YBa₂Cu₃O_{7-δ} nanocomposite thin films *Phys. Rev. Mater.* 1 024801
- [23] Llordés A et al 2012 Nanoscale strain-induced pair suppression as a vortex-pinning mechanism in high-temperature superconductors Nat. Mater. 11 329–36
- [24] Coll M et al 2014 Size-controlled spontaneously segregated Ba₂YTaO₆ nanoparticles in YBa₂Cu₃O₇ nanocomposites obtained by chemical solution deposition Supercond. Sci. Technol. 27 044008
- [25] Talantsev E, Wimbush S, Strickland N, Xia J, D'Souza P, Storey J, Tallon J, Ingham B, Knibbe R and Long N 2013 Oxygen deficiency, stacking faults and calcium substitution in MOD YBCO coated conductors *IEEE Trans. Appl.* Supercond. 23 7200205
- [26] Talantsev E, Strickland N, Wimbush S, Storey J, Tallon J and Long N 2014 Hole doping dependence of critical current density in YBa₂Cu₃O_{7-δ} conductors Appl. Phys. Lett. 104 242601
- [27] Puichaud A, Wimbush S and Knibbe R 2017 Enhanced low-temperature critical current by reduction of stacking faults in REBCO coated conductors *Supercond. Sci. Technol.* 30 074005
- [28] Gauquelin N, Zhang H, Zhu G, Wei J Y T and Botton G A 2018 Atomic-scale identification of novel planar defect phases in heteroepitaxial YBa $_2$ Cu $_3$ O $_{7-\delta}$ thin films AIP Adv. 8 055022
- [29] Zhang H, Gauquelin N, McMahon C, Hawthorn D, Botton G and Wei J 2018 Synthesis of high-oxidation Y-Ba-Cu-O phases in superoxygenated thin films *Phys. Rev. Mater.* 2,033803
- [30] Diez Sierra J, Lopez-Dominguez P, Rijckaert H, Rikel M O, Hänisch J, Khan M Z, Falter M, Bennewitz J, Huhtinen H and Schäfer S 2020 High critical current density and enhanced pinning in superconducting films of YBa₂Cu₃O_{7-δ} nanocomposites with embedded BaZrO₃, BaHfO₃, BaTiO₃ and SrZrO₃ nanocrystals ACS Appl. Nano Mater. 3 5542-53